Iowa Research Online
The University of Iowa's Institutional Repository

Theses and Dissertations

Spring 2018

MRI-based active shape model of the human proximal femur using fiducial and secondary landmarks and its validation

Xiaoliu Zhang
University of Iowa

Follow this and additional works at: https://ir.uiowa.edu/etd

Part of the Electrical and Computer Engineering Commons

Recommended Citation

Zhang, Xiaoliu. "MRI-based active shape model of the human proximal femur using fiducial and secondary landmarks and its validation." MS (Master of Science) thesis, University of Iowa, 2018.
https://doi.org/10.17077/etd.pl67d1u7

MRI-BASED ACTIVE SHAPE MODEL OF THE HUMAN PROXIMAL FEMUR
USING FIDUCIAL AND SECONDARY LANDMARKS AND ITS VALIDATION

by

Xiaoliu Zhang

A thesis submitted in partial fulfillment of the requirements
for the Master of Science degree in Electrical and Computer Engineering
in the Graduate College of The University of Iowa

May 2018

Thesis Supervisor: Professor Punam K. Saha

Graduate College
The University of Iowa
Iowa City, Iowa

CERTIFICATE OF APPROVAL

_____

MASTER'S THESIS

_____

This is to certify that the Master's thesis of

Xiaoliu Zhang

has been approved by the Examining Committee for
the thesis requirement for the Master of Science degree
in Electrical and Computer Engineering at the May 2018 graduation.

Thesis Committee: _____
                   Punam K. Saha, Thesis Supervisor

                   _____
                   Nicole M. Grosland

                   _____
                   Reinhard R. Beichel

                   _____
                   Xiaodong Wu

ACKNOWLEDGEMENTS

This work has been done under the supervision of Prof. Saha. It is my honor to be guided by Prof. Saha on the road of independent research. His insight on new problems, expertize in this field, and patience on instruction help me a lot over the whole process. Moreover, he assures me that it's understandable to make mistakes and encourages me to think boldly. His attitude and words always inspire me to do research in a consistent, peaceful, and innovative way.

Also, I'd like to give my special thanks to Professor Gregory Chang from NYU for providing the data. Whenever I had questions, he would reply in no time, clear my doubts, and make it possible that my research went on smoothly.

I am grateful for all the help I got from my excellent labmates, Cheng Chen, Dakai Jin, Syed Ahmed Nadeem, and Indranil Guha, on my research. And I am also thankful that the incredible faculty and staff I have met at the University of Iowa make my life easier.

Furthermore, I am honored to have Professor Nicole M. Grosland, Professor Reinhard R. Beichel, and Professor Xiaodong Wu on my thesis committee and appreciate the time and efforts they devoted to my thesis.

Finally, I would like to thank my parents for their unconditional support all these years.

ABSTRACT

Osteoporosis, associated with reduced bone mineral density and structural degeneration, greatly increases the risk of fragility fracture. Magnetic resonance imaging (MRI) has been applied to central skeletal sites including the proximal femur due to its non-ionizing radiation. A major challenge of volumetric bone imaging of the hip is the selection of regions of interest (ROIs) for computation of regional bone measurements. To address this issue, an MRI-based active shape model (ASM) of the human proximal femur is applied to automatically generate ROIs. The challenge in developing the ASM for a complex three-dimensional (3-D) shape lies in determining a large number of anatomically consistent landmarks for a set of training shapes. This thesis proposes a new method of generating the proximal femur ASM, where two types of landmarks, namely fiducial and secondary landmarks, are used. The method consists of—(1) segmentation of the proximal femur bone volume, (2) smoothing the bone surface, (3) drawing fiducial landmark lines on training shapes, (4) drawing secondary landmarks on a reference shape, (5) landmark mesh generation on the reference shape using both fiducial and secondary landmarks, (6) generation of secondary landmarks on other training shapes using the correspondence of fiducial landmarks and an elastic deformation of the landmark mesh, (7) computation of the active shape model. A proximal femur ASM has been developed using hip MR scans of 45 post-menopausal women. The results of secondary landmark generation were visually satisfactory, and no topology violation or notable geometric distortion artifacts were observed. Performance of the method was examined in terms of shape representation errors in a leave-one-out test. The mean and standard deviation of leave-one-out shape representation errors were 1.40mm and 0.37mm respectively. The experimental results

iii

suggest that the framework of fiducial and secondary landmarks allows reliable computation of statistical shape models for complex 3-D anatomic structures.

PUBLIC ABSTRACT

Osteoporosis poses a high risk of fragility fracture for people, and hip is one of the most common places where it occurs. Despite the fact that magnetic resonance imaging (MRI) has been applied to central skeletal cites for clinical analysis, a major challenge for computation of regional bone measurements is the selection of regions of interest (ROIs). To automatically generate ROIs, an MRI-based active shape model (ASM) of the human proximal femur is applied. The fundamental work of building an ASM is to determine a set of landmarks. For a complex three-dimensional (3-D) shape like human proximal femur, it's not easy to locate a large number of anatomical consistent landmarks. In this thesis, a new method is proposed to generate the proximal femur ASM, where two types of landmarks, namely fiducial and secondary landmarks, are used. The main idea of this method is to deform the secondary landmarks of a reference shape to the corresponding surface of target shapes by an elastic deformation model, given the relationship of fiducial landmarks between the reference shape and target shapes. Then develop an ASM based on all training shapes. Hip MR scans of 45 post-menopausal women were applied in the experiment. It was observed that secondary landmarks generated from this method were visually satisfactory, and no topology violation or notable geometric distortion artifacts existed. The mean and standard deviation of leave-one-out shape representation errors were 1.40mm and 0.37mm respectively, demonstrating that the framework of fiducial and secondary landmarks is reliable for computation of complex 3-D shape models.

TABLE OF CONTENTS

LIST OF FIGURES

CHAPTER 1
INTRODUCTION

1.1 Background and Motivation

Osteoporosis, associated with reduced bone mineral density (BMD) and structural degeneration of cortical and trabecular bone, greatly increases the risk of fragility fracture ([1]–[3]). Nearly, 40% of women and 13% of men suffer a fragility fracture in their lifetimes ([4]). The continued rise in life expectancy is predicted to increase fracture incidence by three-fold ([5]). Osteoporotic fractures are one of the most common causes of disability, and a major contributor to medical costs ([6]). Osteoporotic hip fractures are especially devastating, reducing life expectancy by 10-20% ([7]), and more than three-quarters of all hip fractures occur in women ([6]).

At present, dual-energy X-ray absorptiometry (DXA) measured areal BMD is used to diagnose osteoporosis. Lately, volumetric imaging including magnetic resonance imaging (MRI) ([8]–[11]), high-resolution peripheral quantitative computed tomography (HR-pQCT) ([12]), and multi-row detector CT (MDCT) imaging ([13]) have drawn interest to measure both bone density and structure. Among these modalities, MRI and MDCT are applicable to central skeletal sites including the proximal femur.

Different groups have applied various methods for topologic and geometric characterization of TB microarchitecture ([14]–[17]). Parfitt *et al.* ([14]) proposed a parallel interconnected trabecular plate model computing TB area and volume fractions, and trabecular spacing and number. Vesterby *et al.* ([15]) introduced the star volume measure, which is the average volume of an object region that can be seen from a point inside that region unobscured in all directions. Hildebrand *et al.* ([16]) formulated the 3-D structure model index, a pseudo-measure of global plate-to-rod ratio, based on the observation that,

for plate-like structure, the rate of volume change with respect to thickness is different from that for rod-like structures. Feldkamp *et al.* ([17]) expressed the makeup of TB networks in terms of topological entities such as the 3-D Euler number.

There is histologic evidence confirming the relationship between the gradual conversion of trabecular plates to rods and increased fracture-risk ([18], [19]). Kleerekoper *et al.* ([18]) observed lower mean TB plate density among individuals with osteoporotic vertebral compression fractures compared with BMD-matched controls without fractures. Recker ([19]) reported reduced trabecular connectivity among patients with vertebral crush fractures as compared to healthy controls with matching TB volume. Recent advancement in digital topology and geometry allows fully automated characterization of individual trabecular plates and rods ([20]–[27]), distinguishing between longitudinal and transverse trabecular structures ([13]), and accurately computing trabecular thickness, spacing ([28]–[31]), and orientation ([13], [32]).

Among others, a major challenge with hip bone image analysis is the selection of regions of interest (ROIs) for regional measurements of bone quality. Toward this goal, we develop an active shape model (ASM) ([33]) of the human proximal femur ([34]), which will be used to automatically generate consistent ROIs. Also, the ASM will be useful to define shape and geometric measures of the femur, and their relationships with fracture risk may be investigated.

Major challenges in developing the ASM of a complex three-dimensional (3-D) shape lie in determining a large number of anatomically consistent landmarks in the training shapes. Although, several research efforts ([35]–[37]) have been made along this direction, the challenges are not yet met. Here, a new method of generating active shape

model of a given 3-D anatomic shape is proposed, where two different types of landmarks, namely fiducial and secondary landmarks, are used. On a 3-D anatomic shape, often, several lines can be defined and manually located with high confidence and reproducibility. Such lines will be used to define fiducial landmarks. Using fiducial landmarks, a large number of secondary landmarks will be generated using a fully automated computational model.

1.2 Research Aims

To achieve the overall goals discussed in the previous paragraph, the follow specific aims were defined for my master's thesis research.

Aim 1: Development of a shape-based morphological smoothing algorithm and apply it on the human proximal femur volume manually segmented from hip MRI.

    a) Compute signed distance transform from the manually segmented proximal femur bone surface.

    b) Apply smoothing on the signed distance transform field using a Gaussian smoothing kernel.

    c) Generate the smooth femur bone volume using a threshold at zero value on the smooth signed distance transform field.

Aim 2: Generation of fiducial landmarks for all training shapes and establishment of a complete set of landmarks for a reference shape.

    a) Define an anatomic landmark system for the human proximal femur bone surface.

    b) Draw fiducial landmarks on the surface of all femur bone shapes.

    c) Draw secondary landmarks on a randomly selected shape, referred to as the reference shape.

d) Build the complete landmark mesh for the reference shape.

Aim 3: Deformation of the reference landmark mesh on to the surface of individual training femur bone shapes using fiducial landmark correspondence.

a) Align pose factors of the reference landmark mesh to the target training shape using fiducial landmark correspondence.

b) Iteratively deform reference fiducial landmarks to their target locations on the target bone surface.

c) Iteratively deform the reference secondary landmark mesh onto the target bone surface using a new geodesic elastic deformation algorithm.

Aim 4: Development and evaluation of an ASM using the complete landmarks of all training shapes.

1.3 Thesis Outline

In Chapter 2, the method to smooth MRI of human proximal femur will be introduced, also the protocol of constructing a landmark system will be explained in detail, the elastic deformation method will be illustrated, and finally the topology condition will be given. In Chapter 3, experiment data and results will be shown. The result of secondary landmark generation, as well as the performance of the ASM by leave-one-out test will be demonstrated. In Chapter 4, the conclusion as well as further discussion is given. Also, long term goals of the related research and future research directions are outlined in Chapter 4.

CHAPTER 2
METHODS

In this chapter, a new framework for computing an MRI-based ASM of the human proximal femur using the notions of fiducial and secondary landmarks ([34]) is presented. Although, the framework is applicable to any 3-D shapes, some of the steps of this method were designed to meet the specific challenges of generating MRI-based femur ASM. Following the guidelines by Cootes *et al.* ([33]), a shape instance $\mathbf{x}_i$ is represented as a vector defining an ordered sequence of n landmark points, i.e. $\mathbf{x}_i = (x_{i,1}, y_{i,1}, z_{i,1}, \cdots, x_{i,n}, y_{i,n}, z_{i,n})^{\mathrm{T}}$. The generation of an active shape model requires a set of training shape instances derived from a shape family, e.g., the MRI-based human proximal femur bone. For the purpose of training, proximal femur bone surface of individual subjects is segmented from MRI. However, the most critical step in the training phase is to locate a large number of landmark points at anatomically consistent locations of individual bone surfaces. The complexity of this step is further enhanced for complex 3-D shapes such as the human proximal femur. A framework to automatically locate the individual landmarks using the correspondence of a significantly reduced number of anatomic features, which can be reliably and reproducibly located on individual femur shapes, is proposed. Such a reliable anatomic feature will be referred to as a "fiducial landmark line." The idea is to use the correspondence of fiducial landmark lines to warp a reference set of a large number of secondary landmark points on to a given training shape; the reference set of secondary landmark points is defined only once on one reference bone shape. Based on this principle, the method of computing the MRI-based femur ASM is accomplished in the following steps—(1) segmentation ([38], [39]) of the femur bone volume; (2) smoothing of the bone surface; (3) drawing of the fiducial landmark lines on

each training shape; (4) drawing of the secondary landmarks on a reference shape; (5) landmark mesh generation on the reference bone shape using both fiducial and secondary landmarks; (6) generation of the secondary landmarks on other training shapes using the correspondence of fiducial landmarks and an elastic landmark mesh deformation; (7) computation of the active shape model using fiducial and secondary landmarks; and (8) validation. After building the active shape model, it will be applied to search the shape in image-frame space, for the purpose of landmark localization, or segmentation. In the rest of this chapter, we describe the theory and algorithms for each of the above steps.

2.1 Segmentation and Smoothing of the MRI-Based Femur Bone Surface

The femur bone boundary was manually traced from MR images under the supervision of an expert radiologist on each axial image slice (Figure 1(a)) using the Firevoxel (https://wp.nyu.edu/firevoxel/) graphical tool. The segmentation result of a proximal femur shape is shown in Figure 1(b). Due to the limited image resolution of the hip MRI and slice-by-slice approach of manual outlining, the segmented femur bone suffered from digital staircase artifacts; see Figure 1(b). It is important to eliminate such artifacts before drawing the landmark lines on the femur surface because such irregularities may add artifactual variabilities in the computed ASM. A new algorithm to smooth a digital bone surface is introduced.

The new smoothing algorithm is developed along the principle of shape-based interpolation ([40]). First, a signed distance transform is computed such that its magnitude represents the distance from the femur surface, while its sign indicates whether a voxel is inside (positive) or outside (negative) the femur volume. Next, a linear interpolation of the signed distance transform field is applied to generate a high-resolution isotropic image,

which is followed by a smoothing step using a Gaussian smoothing kernel. Finally, the high-resolution femur bone volume with a smooth surface is computed by thresholding the smooth distance field at '0'. This smoothing algorithm is referred as a morphologic smoothing algorithm. The result of morphologic smoothing of the femur bone surface of Figure 1(b) is shown in Figure 1(c). For all subsequent steps, high-resolution smooth femur bone surfaces are used to generate the femur ASM.
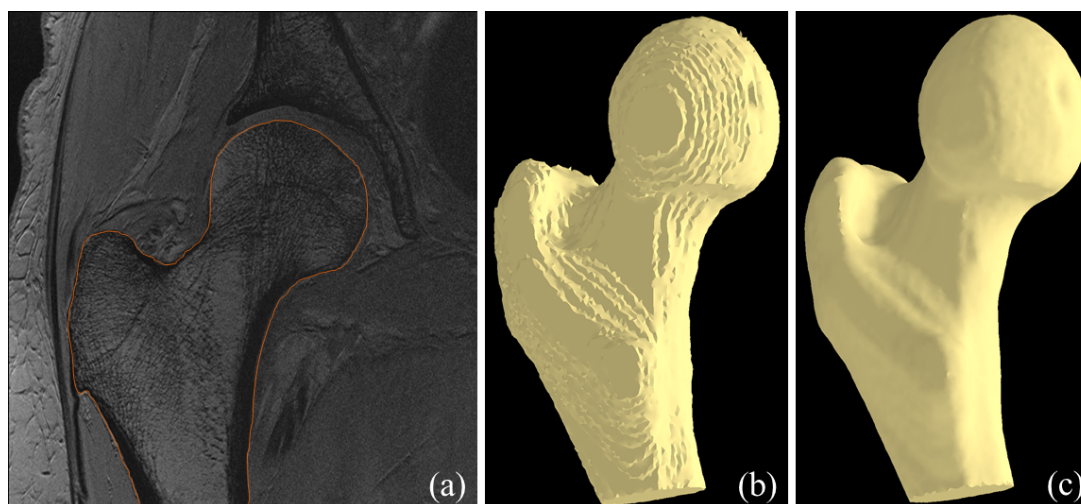
Figure 1. Illustration of MRI-based human proximal femur bone shape. (a) An axial image slice from a hip MR image. The femur bone boundary was manually traced (red line) through the graphical user interface supported by the Firevoxel software tool (https://wp.nyu.edu/firevoxel/). (b) Segmented femur volume using manual outlining of the femur bone boundary on individual axial image slices. (c) Femur bone surface after applying the morphologic smoothing algorithm.

2.2 Development of Landmark Systems

Generating landmarks on individual training shapes is accomplished in two steps — (1) location of fiducial landmarks based on reliable anatomic features and (2) generation of secondary landmarks based on the correspondence of fiducial landmarks. The fiducial

landmarks are manually drawn on individual training bone surfaces as per a pre-defined reference of anatomic fiducial lines (blue lines in Figure 2). A prototype of secondary landmarks is manually defined on a reference shape, which is warped onto individual training shapes using the correspondence of fiducial landmarks.

2.2.1 Fiducial Landmark System

The fiducial lines are defined based on the anatomic features of the shape family. Also, it is required that the fiducial lines divide the entire bone surface into multiple simply-connected regions ([41]). Initially, a fiducial line is drawn as a curve on the bone surface. A fiducial landmark line (or, 'landmark line' in short) is generated by computing a sequence of a predefined number of equidistant fiducial landmarks on the fiducial line. Let us assume that a shape is represented by l fiducial landmark lines $L_1, L_2, \cdots, L_l$ and generating r regions $R_1, R_2, \cdots, R_r$. It may be noted that a region R is bounded by a set of landmark lines; let $\Gamma(R_i)$ denote the set of bounding fiducial landmark lines for the region R_i. A landmark line L_i is a sequence of fiducial landmarks $\langle \mathbf{f}_1, \mathbf{f}_2, \cdots, \mathbf{f}_{n_i} \rangle$, where $\mathbf{f}_1$ and $\mathbf{f}_{n_i}$ are end-landmarks. In this thesis, lowercase bold-face letters are used to denote a point or landmark. To ensure that the landmark lines divide the bone surface into topologically consistent regions, it is required that two landmark lines L_i and L_j intersect only at their end-landmarks, and an end-landmark is shared by at least three landmark lines.

Fiducial lines and landmarks on a specific training sample are illustrated in Figure 2. Fiducial lines were manually drawn on an MRI-derived smooth proximal femur bone surface to denote clinically important anatomic regions including the femoral head, neck, greater trochanter, and intertrochanteric region, which correspond to the most common locations of osteoporotic fractures in the proximal femur. Fiducial lines were also placed

to divide complex regions into relatively simpler sub-regions facilitating robust elastic deformation during the generation of secondary landmarks. Fiducial landmarks were drawn on individual training shapes using a custom designed graphical user interface (GUI) developed in our laboratory to interactively locate fiducial landmark lines on the femur bone surface. Conventional GUI systems provide graphical interface functions to manipulate points, lines, and curves on a 2-D plane. Our custom designed GUI system, called a geodesic editor ([42]), enables a user to directly interact on a geodesic surface facilitating landmark location on anatomic shapes. Also, the GUI facilitates the landmark generation process by assigning an identification number to each fiducial landmark line so that the correspondence of landmark lines among individual training shapes are maintained. Finally, the fiducial landmarks (points) are generated by uniformly sampling a predefined number of points on each fiducial line.
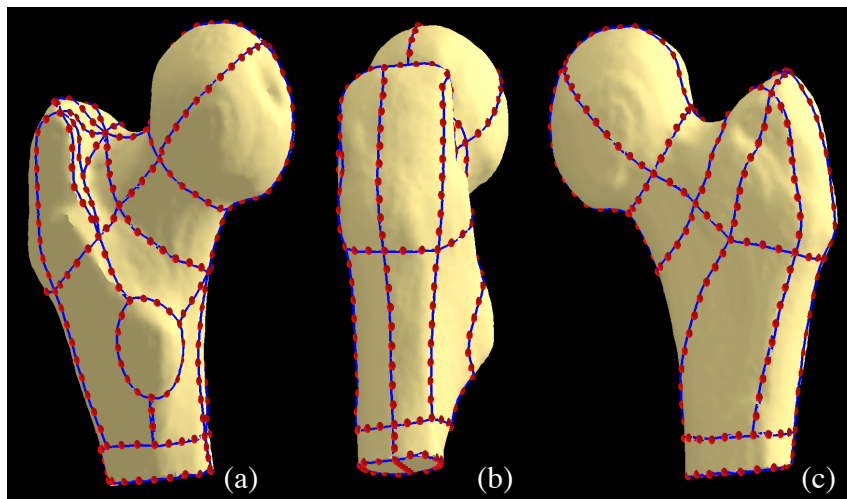

Figure 2. Illustration of fiducial lines (blue) and landmarks (red) on a specific femur bone training shape generated from a hip MRI. Fiducial landmarks on the same femur shape are shown from three different viewing angles.

2.2.2 Secondary Landmark System

A prototype of secondary landmarks is generated on a specific training shape referred to as the reference shape. The idea here is to warp the secondary landmarks on to individual training shapes using the correspondence of fiducial landmarks of the reference and specific training shapes. This step is crucial for reducing user time and more importantly for avoiding human errors in placing a large number of landmarks at anatomically consistent locations.
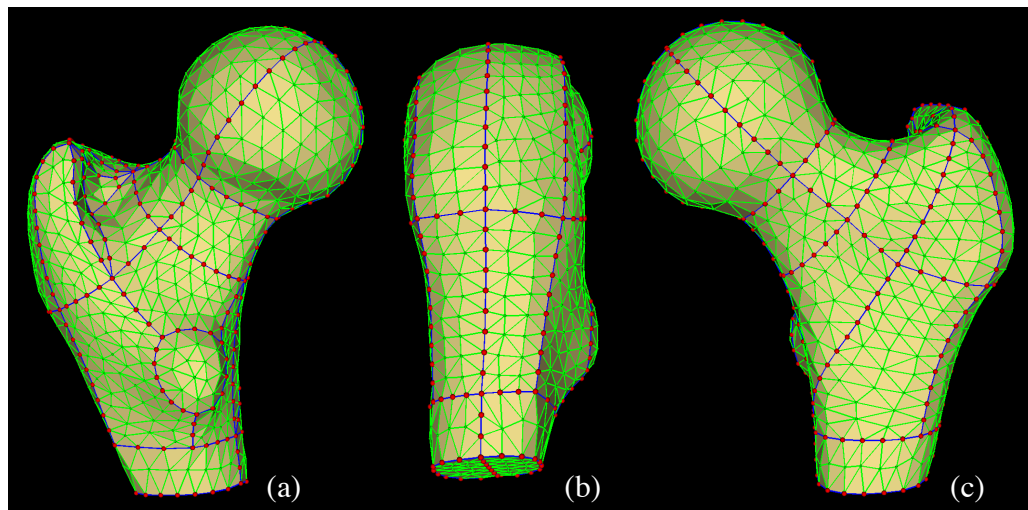
Figure 3. Illustrations of secondary landmarks. Manually added secondary landmarks (green dots) on the reference training shape are shown along with the landmark mesh. Fiducial landmarks are shown in red, while the edges on a fiducial landmark line are shown in green.

A random shape from the training data set is chosen as the reference shape. The secondary landmarks are manually drawn on the reference shape at a quasi-uniform distribution. Finally, the landmark mesh involving both fiducial and secondary landmarks is computed using the geodesic Voronoi neighborhood and Delaunay triangulation approaches ([41], [43]). The secondary landmarks and the landmark mesh on the reference

training shape are shown in Figure 3. Note that a secondary landmark s belong to a specific region, say R_i; we will refer R_i as the parent region of s.

2.3 Deformation of Reference Landmark Mesh on Individual Training Shapes

As mentioned earlier, the secondary landmarks are not manually located on individual training shapes. Instead, the secondary landmarks are computationally warped on a target training shape using the correspondence of fiducial landmarks and a geodesic spring mesh deformation method. In this section, it will be explained in detail about how to deform the prototype secondary landmarks of the reference training shape on to a target training shape. The method begins with an affine transformation on the prototype secondary landmarks, which is computed using the Procrustes analysis ([44]) and the correspondence among the fiducial landmarks of the reference and target training shapes. The results of the optimum affine transformation on the prototype secondary landmarks is shown in Figure 4.

As observed from the figure, the residual distance between corresponding fiducial landmarks of the reference and target shapes are small for some regions, while the distance is large for certain regions. Also, the distance of secondary landmarks from the target bone surface may be large. The final alignment of the fiducial landmarks of reference and target training shapes and the mapping of the secondary landmarks on to the surface of the target shape is accomplished using a new geodesic spring mesh deformation method, where the secondary landmarks deform under two forces — (1) spring-mesh force and (2) surface-distance force.

Several challenges were observed while formulating the deformation process. For example, often, a situation occurs where a secondary landmark gets closer to a region of

the target surface that is different from its parent region, and therefore, the surface distance force pulls the concerned landmark in a wrong direction. A weak surface-distance force fails to pull the landmark mesh on to the target surface, while a strong surface-distance force prematurely pulls individual landmarks and arrests any further deformation under the spring mesh. Topology violation of the landmark mesh is another major concern during the deformation process. In the following, we describe our geodesic deformation method that overcomes these challenges.
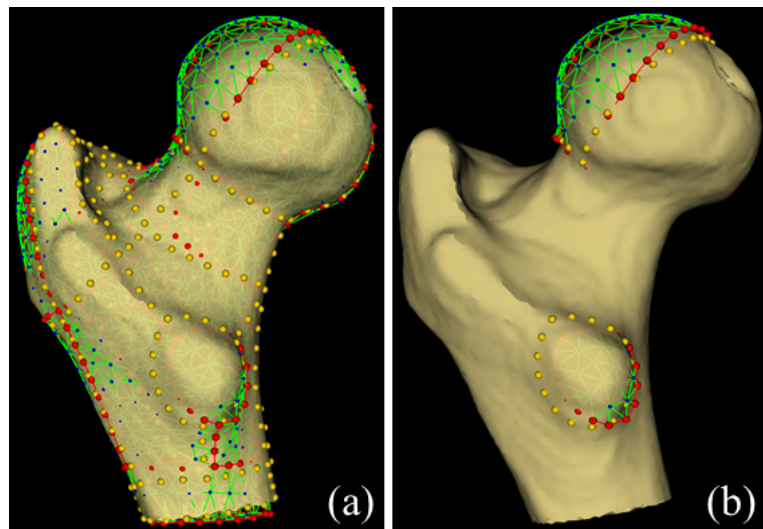
Figure 4. Display of affine transformation result. (a) The result of affine transformation of the reference landmark mesh on a target training bone surface. The fiducial and secondary landmarks on the reference training shape after affine transformation are shown in red and blue, respectively, while the fiducial landmarks on the target bone surface are shown in gold. The target bone surface is displayed with partial transparency. Note that the target shape only has the fiducial landmarks. (b) Same as (a) except that the landmarks of only two disjoint regions are shown for better visualization.

Let $\mathbf{f}_i(0)$ denote a reference fiducial landmark after affine transform and $\dot{\mathbf{f}}_i$ denote its location on the target shape surface. We use $\mathbf{f}_i(t)$ to denote the location of $\mathbf{f}_i(\cdot)$ during the deformation process. The entire deformation process is accomplished in two phases.

During the first phase, each fiducial landmark $\mathbf{f}_i(t)$ is gradually moved toward its target location $\dot{\mathbf{f}}_i$. Specifically, during an iteration of this phase, $\mathbf{f}_i(t)$ is moved to $\mathbf{f}_i(t) + \left(\dot{\mathbf{f}}_i - \mathbf{f}_i(t)\right)/n_0$, where n_0 is the number of iterations for the first phase. After moving all fiducial landmarks during each iteration, the secondary landmarks are allowed to move and stabilize. During the deformation of secondary landmarks, both spring-mesh and surface-distance forces are applied. To overcome the first challenge mentioned in the previous page, different regions of the target bone surface are segmented using the minimum cost geodesic paths on the target bone surface through fiducial landmarks, and it is ensured that a secondary landmark is only pulled toward its parent region. A concept of 'cushion' is introduced in the formulation of surface-distance force to ensure that, during early stages of deformation, the landmark mesh can glide under spring mesh force inside the 'cushion zone,' while surface-distance force ensures that landmarks do not move far from the cushion zone.

During the second phase of the deformation, the cushion value is gradually reduced pulling the landmarks on to the target surface, while escaping a premature halt of spring deformation due to seizure of a landmark on the discrete target surface mesh.

In the following subsections, different forces are defined for the elastic deformation model and the conditions for topology preservation during deformation are demonstrated in detail.

2.3.1 Spring Force

The landmark mesh is modelled as a spring mesh system, where each edge represents a spring and each triangle represents an elastic surface that tends to maintain its original area. After the affine transformation of the reference landmark mesh, spring mesh is considered to be at its relaxed state. As the fiducial landmarks start moving, it perturbs the relaxed state.

Here, we use t to denote a time variable and $t = 0$ right after the affine transformation of the reference landmark mesh. Let $\mathbf{s}(t)$ denote the current location of a secondary landmark, and let $\mathbf{s}_i(\cdot) \mid i = 1, 2, \cdots, m$ be the neighboring landmarks (fiducial or secondary) of $\mathbf{s}(\cdot)$, i.e., each $\mathbf{s}_i(\cdot)$ is directly connected to $\mathbf{s}(\cdot)$ by an edge denoted as $\mathbf{ss}_i(\cdot)$. The total edge spring force on the secondary landmark $\mathbf{s}(t)$ is defined as follows:

$$\mathbf{F}_{\text{edge}}(\mathbf{s}, t) = k_{\text{edge}} \sum_{i=1}^{m} \frac{|\mathbf{ss}_i(t)| - |\mathbf{ss}_i(0)|}{|\mathbf{ss}_i(0)|} \mathbf{i}_{\mathbf{ss}_i(t)}, \tag{1}$$

where k is a spring constant and $\mathbf{i}_{\mathbf{ss}_i(t)}$ is the unit vector from $\mathbf{s}(t)$ to $\mathbf{s}_i(t)$.

Also, each triangle, say $A_i \mid i = 1, 2, \ldots, l$, sharing the vertex $\mathbf{s}(t)$ asserts an area-defined force on $\mathbf{s}(t)$; let $a_i(t)$ denote the area of A_i at t and $\mathbf{i}_{\mathbf{s}A_i(t)}$ denote the unit vector along the inner angular bisector of A_i at its vertex $\mathbf{s}(t)$. The total area based elastic force on $\mathbf{s}(t)$ is defined as follows:

$$\mathbf{F}_{\text{area}}(\mathbf{s}, t) = k_{\text{area}} \sum_{i=1}^{l} \frac{a_i(t) - a_i(0)}{a_i(0)} \mathbf{i}_{\mathbf{s}A_i(t)} \tag{2}$$

Finally, the total spring force on $\mathbf{s}(t)$ is computed by adding both edge- and area-based forces as follows:

$$\mathbf{F}_{\text{spring}}(\mathbf{s}, t) = \mathbf{F}_{\text{edge}}(\mathbf{s}, t) + \mathbf{F}_{\text{area}}(\mathbf{s}, t) \tag{3}$$

2.3.2 Surface-Distance Force

A surface-distance force is applied on each secondary landmark to pull it on to the target bone surface. This force is defined by the distance between the landmark and the target surface. Let $P(\mathbf{s}(t))$ denote the projected point of the moving secondary landmark $\mathbf{s}(t)$ on its parent region R in the target bone surface. The target surface is computationally represented as a discrete triangular mesh and the point $P(\mathbf{s}(t))$ is always projected at a vertex of the mesh. It introduces a discrete nature in the spring mesh deformation, especially, when the surface distance force is strong. Specifically, it stops a spring mesh to deform under the spring force system along the target surface. To overcome this challenge, we introduce a notion of cushion to simulate a surface-distance force-free zone around the target surface so that spring mesh can freely deform inside the cushion zone. The magnitude of the surface-distance force is defined as follows:

$$\mathbf{F}_{\text{surface-distance}}(\mathbf{s}, t) = k_{\text{surface-distance}} \times f_+\big(D(\mathbf{s}(t)) - c\big), \tag{4}$$

where, $k_{\text{surface-distance}}$ is the surface-distance force constant; $f_+(\cdot)$ is a function that returns the input value when it is positive and zero otherwise; $D(\mathbf{s}(t))$ computes the distance between the landmark $\mathbf{s}(t)$ and its parent region R on the target surface; and c is the cushion parameter.

The orientation of the surface-distance force is defined so that the force applied along the inward or outward normal of the spring mesh surface toward reducing the distance between the landmark and its parent surface region on the training shape. However, it is difficult to define the surface normal for a mesh surface. Therefore, we use the unit vector $\mathbf{i}_{\mathbf{s}(t)}$ from $\mathbf{s}(t)$ to the center of gravity of the neighbors. Let $\mathbf{s}_i^n(t)| i = 1,2,\cdots,m$ denote the neighbors of $\mathbf{s}(t)$. Let $\hat{\mathbf{i}}_{\mathbf{s}(t)}$ denote the unit vector from $\mathbf{s}(t)$ to the

nearest point on its parent region R. Finally, the direction of the surface-distance force $\mathbf{F}_{\text{surface-distance}}(\mathbf{s}, t)$ is used as $\mathbf{i}_{\mathbf{s}(t)}$ or $-\mathbf{i}_{\mathbf{s}(t)}$ depending on the sign of the inner product of $\mathbf{i}_{\mathbf{s}(t)}$ and $\hat{\mathbf{i}}_{\mathbf{s}(t)}$. If it's positive, the direction of $\mathbf{F}_{\text{surface-distance}}(\mathbf{s}, t)$ is the same as $\mathbf{i}_{\mathbf{s}(t)}$. Otherwise, it's in the reverse direction of $\mathbf{i}_{\mathbf{s}(t)}$.

Finally, the total force on a secondary landmark $\mathbf{s}(t)$ is defined as follows:

$$\begin{aligned} \mathbf{F}_{\text{total}}(\mathbf{s}, t) &= \mathbf{F}_{\text{spring}}(\mathbf{s}, t) + \mathbf{F}_{\text{surface-distance}}(\mathbf{s}, t) \\ &= \mathbf{F}_{\text{edge}}(\mathbf{s}, t) + \mathbf{F}_{\text{area}}(\mathbf{s}, t) + \mathbf{F}_{\text{surface-distance}}(\mathbf{s}, t). \end{aligned} \tag{5}$$

2.3.3 Topology Preservation Constraints

During the deformation process it is necessary to constantly check that the mesh topology is not violated. During a mesh deformation a topology is violated when two independent mesh structures intersect each other. Two mesh structures are independent if their intersection is empty, i.e., they share no common structure. Different cases of topology violations may occur — (1) a vertex intersects an independent vertex, edge or triangle, which are shown in Figure 5(a)-(c); and (2) an edge cuts through another independent edge or triangle. Topology violations caused by a vertex intersecting an independent mesh element are easy to visualize. An example of topology violation, where an edge cuts through another independent edge is shown in Figure 5(d).

To avoid topological violations during mesh deformation, it is ensured that two independent mesh structures never come too close. Specifically, to check that a vertex v (or, an edge E) does not come to the vicinity of another independent mesh structure, for each mesh triangle T, it's necessary to check the following two conditions: (1) The distance between v (or, E) and the plane P_T containing T is larger than δ, and (2) the projection v_T (or, E_T) of v (respectively, E) on P_T is more that δ distance away from T.

A sufficiently small movement of v does not cause mesh topology violation with respect to a triangle T and the edge and vertices of T, if any of the above two conditions holds for v and all edges connected to v. The distance threshold should be significantly greater than individual movement steps of mesh vertices. Since, the spring mesh deformation is defined by a force model, the possible movements of individual vertices may cover a wide range of distances. Therefore, the following strategy is adopted.

First, the displacement vector $\mathbf{d}$ of a given vertex v during an iteration is determined using the underlying force model. The application of computed displacement $\mathbf{d}$ on v is accomplished in $\lceil |\mathbf{d}|/\delta_{\mathbf{d}} \rceil$ number of sub-iterations, where $\lceil \cdot \rceil$ is the ceiling operator; $\delta_{\mathbf{d}} \ll \delta$ is the constant micro-displacement length applied during each sub-iteration. During each sub-iteration, a displacement of $\delta_{\mathbf{d}} \mathbf{d}/|\mathbf{d}|$ is applied on the vertex v under the constraint of topology preservation.

Topology preservation checking is applied at each sub-iteration, and it involves significant computation with all mesh triangles, which is a large number; for example, the landmark mesh used for our experiments had 1712 mesh triangles. Therefore, an efficient implementation of topology preservation is needed to practically solve the deformation process. In our algorithm, a data structure is created to keep track of the set of independent mesh tringles spatially nearby to a specific vertex. Also, we keep track of cumulative displacements for each vertex since the last update of its nearby tringle data structure. Finally, this data structure for a specific vertex is updated after its cumulative displacement exceeds a threshold.
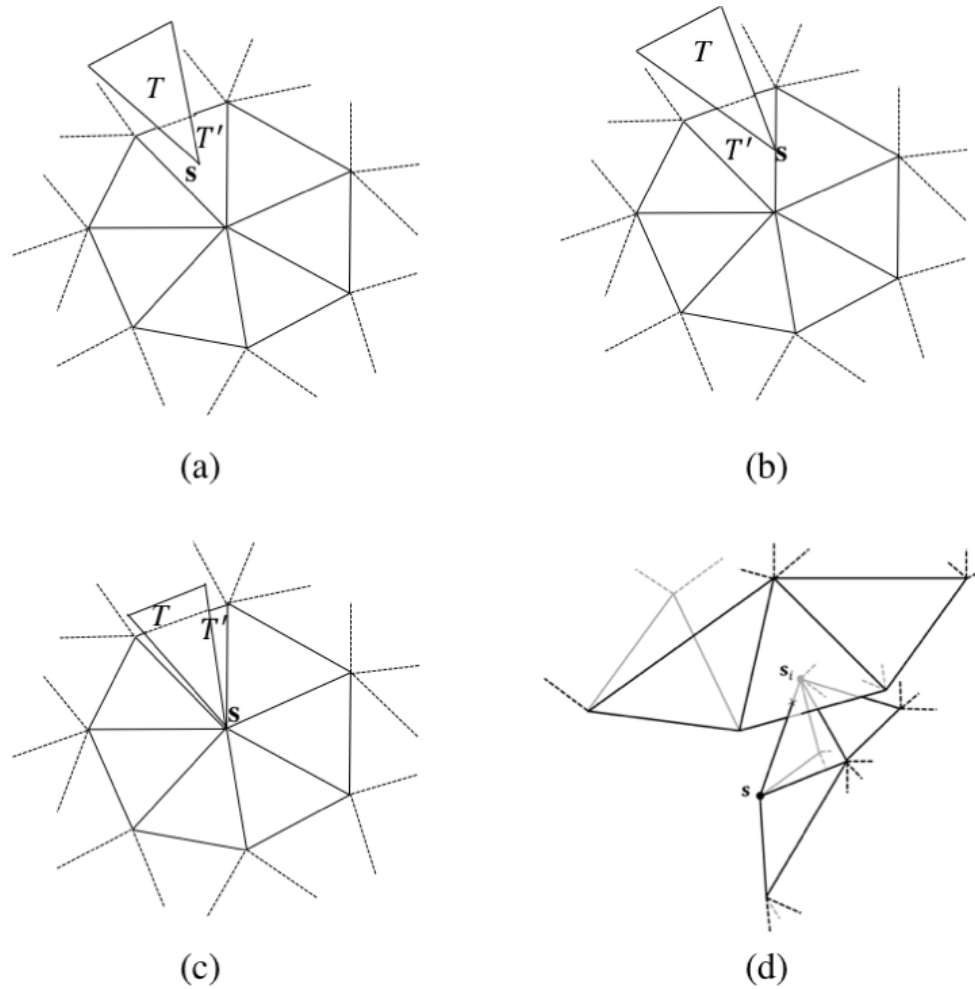
Figure 5. Different cases of topology violation. (a-c) A vertex **s** of triangle T locates inside the face, on an edge, at a vertex of a triangle T' respectively. (d) An example where an edge (**ss**$_i$) cuts through another independent edge to trigger a topology violation. Visible edges are shown in black while invisible edges are shown in light gray. The vertex **s**$_i$ is on the other side of the independent triangle through which the edge **ss**$_i$ intersects and is not visible. It may be noted that both vertices **s** and **s**$_i$ may be significantly far from the intersection triangle, and therefore, may not be detected using the first condition of topology preservation. It may be noted that such case of topology violation is not frequent and easy to be overlooked.

2.4 Development of Active Shape Model

Following the framework proposed by Cootes and Taylor ([33]), the mean and variation in an anatomic shape can be computed after eliminating the pose variations among training shapes through the Procrustes method and then performing a principal component analysis (PCA) to capture the nonlinear shape variation among training shapes. Let us assume that the shape of a bone surface is represented by N landmarks. Thus, a femur shape requires a $3N$ dimensional vector and an active shape model of a femur is expressed by the following equation:

$$\mathbf{a} = \mathbf{\mu} + P\mathbf{b}, \tag{5}$$

where $\mathbf{a}$ is a shape instance; $\mathbf{\mu}$ is the mean shape; P is a matrix of k eigenvectors corresponding to the k largest eigenvalues computed using the PCA of training shapes after eliminate pose variations using the Procrustes method; and $\mathbf{b}$ is a k dimensional vector representing the shape-control parameters.

2.5 Shape Optimization on a Segmented Femur Bone Surface

The compute the optimum shape instance from an ASM to fit the surface of segmented proximal femur bone from a MR image, an image search method has been developed that is based on the principle originally proposed by Cootes and Taylor [33]. This method starts with the mean shape, i.e., the shape parameter $\mathbf{b} = \mathbf{0}$ and an initial set of pose parameters orientation (azimuth and elevation) $\mathbf{\theta}$, scale s, and translation $\mathbf{T}_c$. Then, it iteratively update the shape instance using the following steps – (1) determine the next possible landmark locations based on image information, (2) modify the linear pose parameters to best accommodate the new landmark locations, and (3) revise the nonlinear

shape parameters to best accommodate the new landmark locations after adjustment of pose parameters. These iterations are continued until convergence.

In this thesis, a method based on distance transform has been developed to help find the next possible locations for landmarks during an iteration. Specifically, the method computes the distance transform as follows. Let V denote the segmented femur bone volume and $\bar{V} = Z^3 - V$, where Z^3 is the image space denote the background. For each voxel $p \in V$, the distance transform value $DT(p)$ is computed as the minimum distance of p from $\bar{V}$, while each voxel $p \in \bar{V}$, the distance transform value $DT(p)$ is computed as the minimum distance of p from V. Thus the computed distance transform field has small values near the femur bone surface and higher values as moved farther from the surface. This distance field is used to determine the next possible landmark locations during an iteration. Specifically, a landmark location $\mathbf{s}$ is moved to the image voxel location in the $3 \times 3 \times 3$ neighborhood of $\mathbf{s}$ with the smallest distance transform value. In other words, the next location of $\mathbf{s}$ is moved closer to the femur surface boundary. Subsequently, the proposed method by Cootes ([33]) are used to update the pose and shape parameters during an iteration. The process terminates when the average square sum of distance transform values at landmark locations converges.

CHAPTER 3
EXPERIMENTS

The elastic deformation method was applied on hip MR scans of 45 post-menopausal women to achieve the secondary landmark locations, as well as the topology information for all shapes. Second, an ASM was built based on all landmark meshes and tested using leave-one-out strategy. Finally, the ASM built in previous step will be applied to search the shape in image-frame space.

3.1 MR Imaging and Subject Description

MR imaging of 45 postmenopausal women were collected at the New York University. This study had institutional review board approval and was Health Insurance Portability and Accountability Act (HIPAA)–compliant. Written informed consent was obtained from all subjects. From the osteoporosis center at the New York, 45 postmenopausal women were recruited who had femoral neck or total hip BMD T scores of greater than -2.5 (median age: 65.0 years; interquartile range [IQR]: 57.0–70.0 years; median body mass index: 23.2 kg/m2; IQR: 20.9–26.2 kg/m2). ([45])

All subjects were scanned in feet-first supine position on a 3-T MR imager (Skyra; Siemens, Erlangen, Germany) by using a 26-element radiofrequency coil setup (three rows of six elements from the Siemens commercial flexible array coil, two rows of four elements from the Siemens commercial spine coil) to detect the MR signal ([46]). Data from individual coil elements were combined by using the sum-of-squares method. Multichannel arrays are known to provide higher signal-to-noise ratios, which can be used to decrease image voxel size (i.e., increase spatial resolution of the image) and improve image quality ([47], [48]). We acquired high-spatial-resolution images of bone microarchitecture of the entire proximal femur in a slightly oblique coronal plane parallel to the femoral neck by

using a three-dimensional fast low-angle shot sequence (repetition time msec/echo time msec, 31/4.92; flip angle, 25°; matrix, 512 × 512; field of view, 120 mm; in-plane voxel size, 0.234 × 0.234 mm; section thickness, 1.5 mm; number of coronal sections, 60; acquisition time, 25 minutes 30 seconds; bandwidth, 200 Hz/pixel) similar to that used in prior studies performed at peripheral skeletal sites ([49], [50], [51]).

3.2 Results of Deformation

A few examples of landmark mesh for different femur bone shapes are displayed in Figure 6. The bones shapes are similar in the whole while differences exist in certain regions. The results of secondary landmark generation were visually satisfactory, well capturing the features of individual shapes, and no topology violation or notable artifacts were observed.

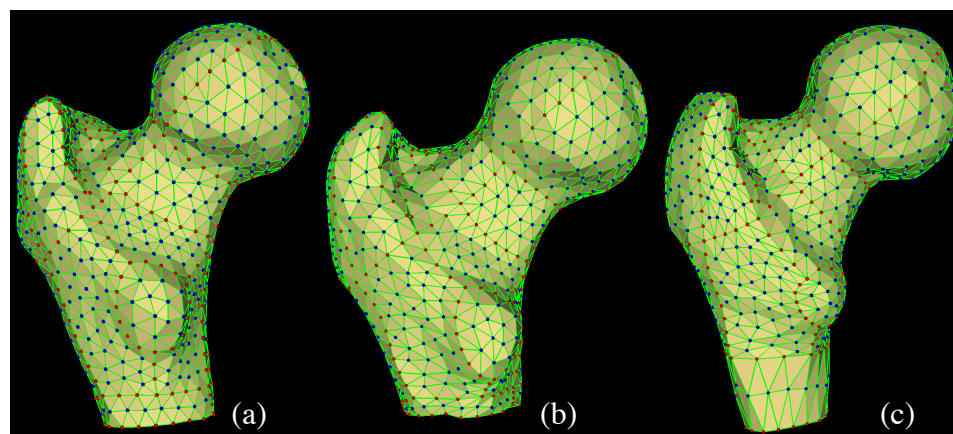Figure 6. Examples of deformation results. Red points denote fiducial landmarks, while blue points represent secondary landmarks. All edges are marked in green.

Results of intermediate steps of secondary landmark generation on a target training shape at different cushion values of FDT-based surface force are shown in Figure 7. The gradual change in the cushion value of the surface distance transform slowly pulls the

secondary surface mesh on to the target surface without adding any distortion artifacts in the deformed landmark mesh.
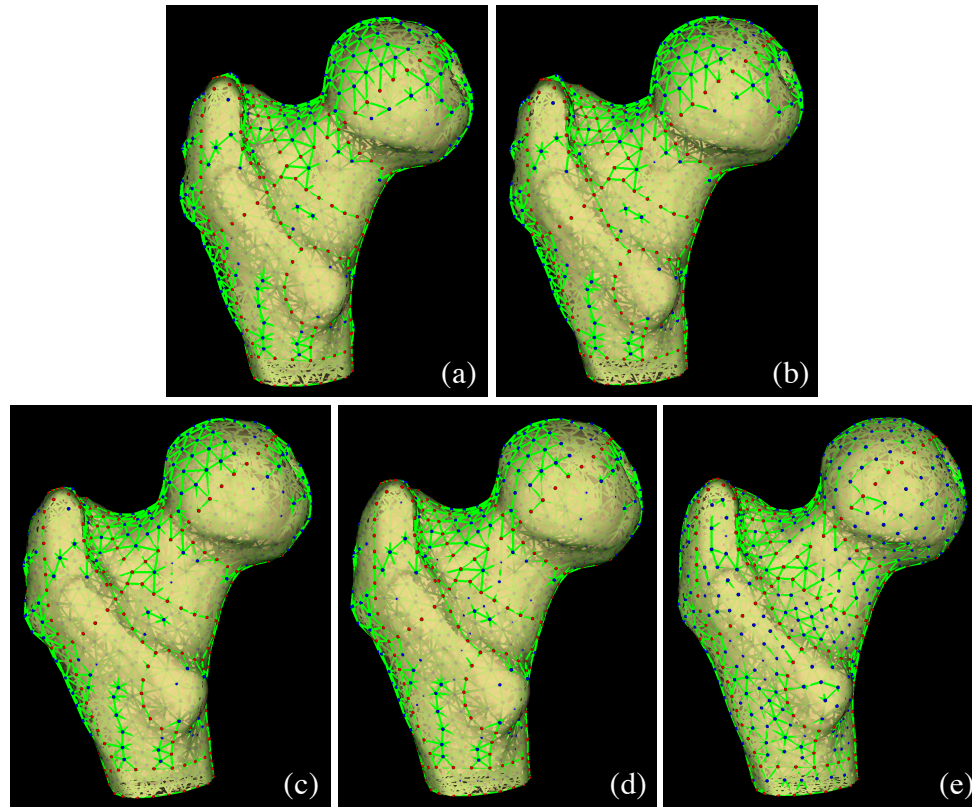

Figure 7. Results of intermediate steps of secondary landmark mesh deformation on a target training shape using spring and surface distance forces. (a-e) Deformation results at cushion values of 1.5, 1.0, 0.5, 0.25, and 0.0, respectively, for the surface distance force.

3.3 Validation of ASM

The landmark representations of all 45 training shapes were used to generate an MRI-based shape model of human proximal femur bone. The PCA of the vector representations of the 45 landmark shapes were performed after affine alignment of the shape using the Procrustes method to eliminate linear pose variation as suggested by Cootes *et al*. ([33]) A total of nineteen effective eigenvectors or shape variation modes corresponding to the largest nineteen eigenvalues were selected to define the MRI-based

human femur shape model, see Figure 8. Variations of femur shapes due to the changes in the first three shape modes are illustrated in Figure 9.
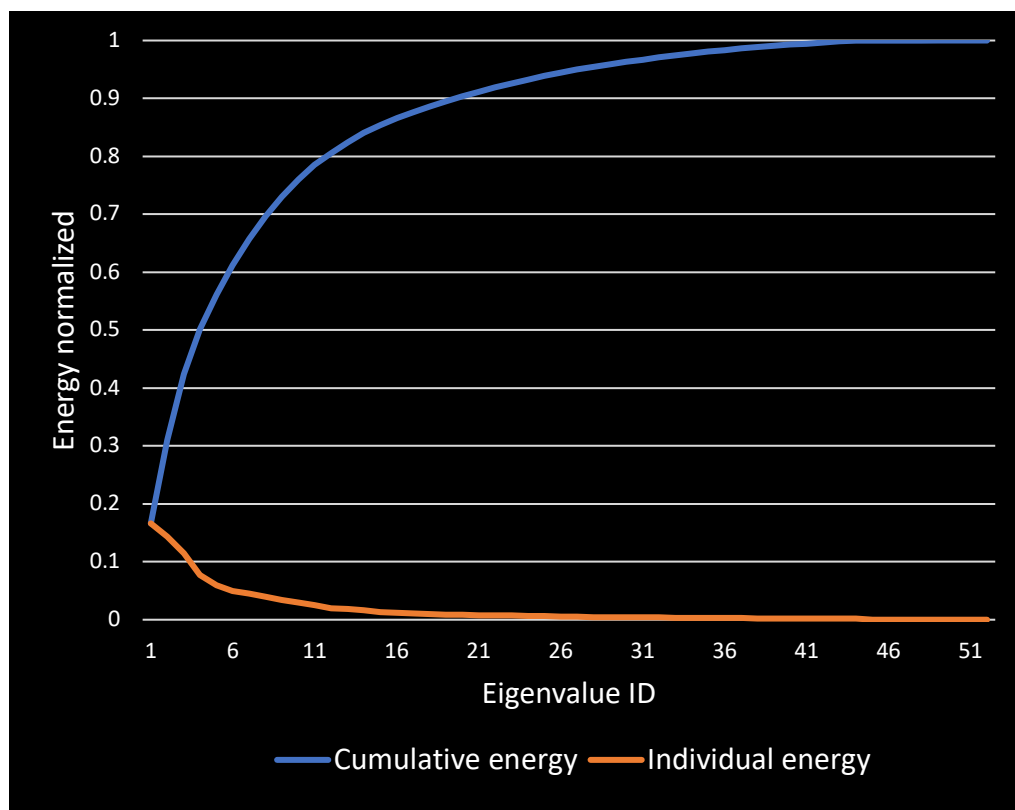

Figure 8. Variation Energy Distribution. The orange curve represents the individual energy, while the blue curve represents the cumulative energy.
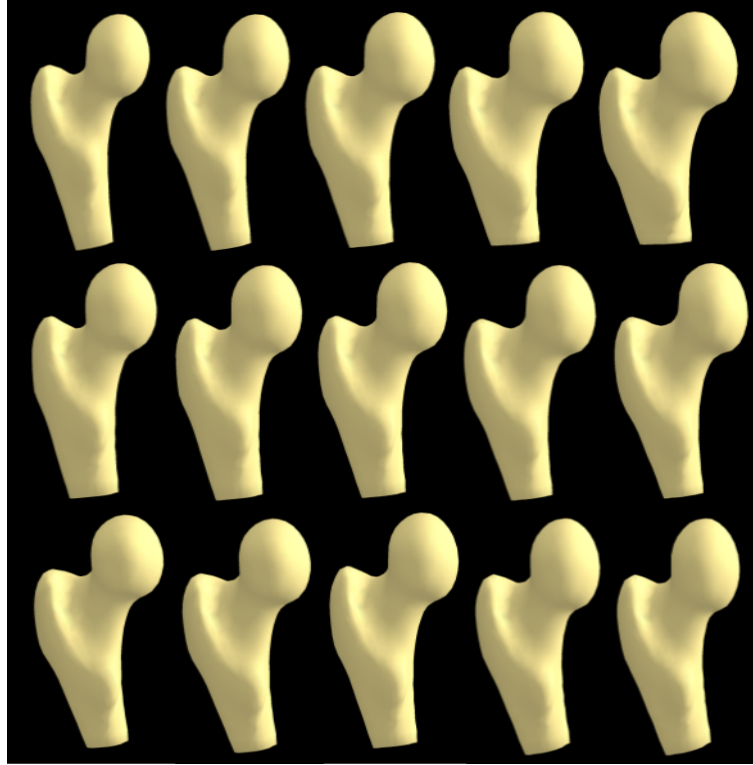
Figure 9. Variations in MRI-based human femur shapes by changing the shape-control parameter along the first three shape modes. The rows from the top represent shape variation due to changes in the 1st, 2nd, and 3rd major shape modes or eigenvectors. On each row, the figures represent the shape instances of mean shape varying at -3, -1,0,1, and 3 times eigenvalue for the corresponding eigenvector.

To test the effectiveness of the computed femur shape model, a leave-one-out test was conducted, and an error analysis was performed as described in the following. Let $\boldsymbol{\alpha}_1, \boldsymbol{\alpha}_2, \cdots, \boldsymbol{\alpha}_{45}$ denote the 45 training shape vectors derived from the 45 MR images used in our experiment. For the leave-one-out test, 45 different leave-one-out active shape models $ASM_1, ASM_2, \cdots, ASM_{45}$ were computed, i.e., ASM_i was computed from the 44 training shapes $\boldsymbol{\alpha}_1, \boldsymbol{\alpha}_2, \cdots, \boldsymbol{\alpha}_{i-1}, \boldsymbol{\alpha}_{i+1}, \cdots, \boldsymbol{\alpha}_{45}$ excluding the training shape instance $\boldsymbol{\alpha}_i$. The best-fit representing of $\boldsymbol{\alpha}_i$ captured by ASM_i was computed by finding the nearest point

projection α_i' of α_i on to the shape subspace of ASM_i represented by its shape matrix after adjusting for the linear pose variation of α_i; let α_i'' denote the linear pose adjusted representation of α_i. Finally, the error of ASM_i in capturing the shape instance α_i was computed as the Euclidean distance between α_i' and α_i'' in the $3N$ dimensional shape space; note that N is the total number three-dimensional landmarks used to represent a femur shape. The max values of the shape representation errors observed in the leave-one-out test was 2.48 mm, while the mean and standard deviation of errors were 1.40 mm and 0.37 mm, respectively.

Another validation experiment was performed to evaluate the performance of the computed ASM to fit with a segmented femur bone surface in an image voxel grid representation. Again, a leave-one-out test was conducted similar to the one described in the previous paragraph. The performance measure or matching error was computed as the average distance transform value at optimized ASM landmark locations from the femur bone surface. Three examples of ASM fitting on the target femur bone surface with low, medium and high matching errors are shown in Figure 10. The statistical analysis shows that the mean distance of optimized shape instances to corresponding femur bone boundary is 0.577 mm and the standard deviation is 0.236 mm. As described in Chapter 4, my future research will be to further optimize the algorithm for shape instance fitting for a target bone surface in the voxel grid without any prior indication of landmarks.
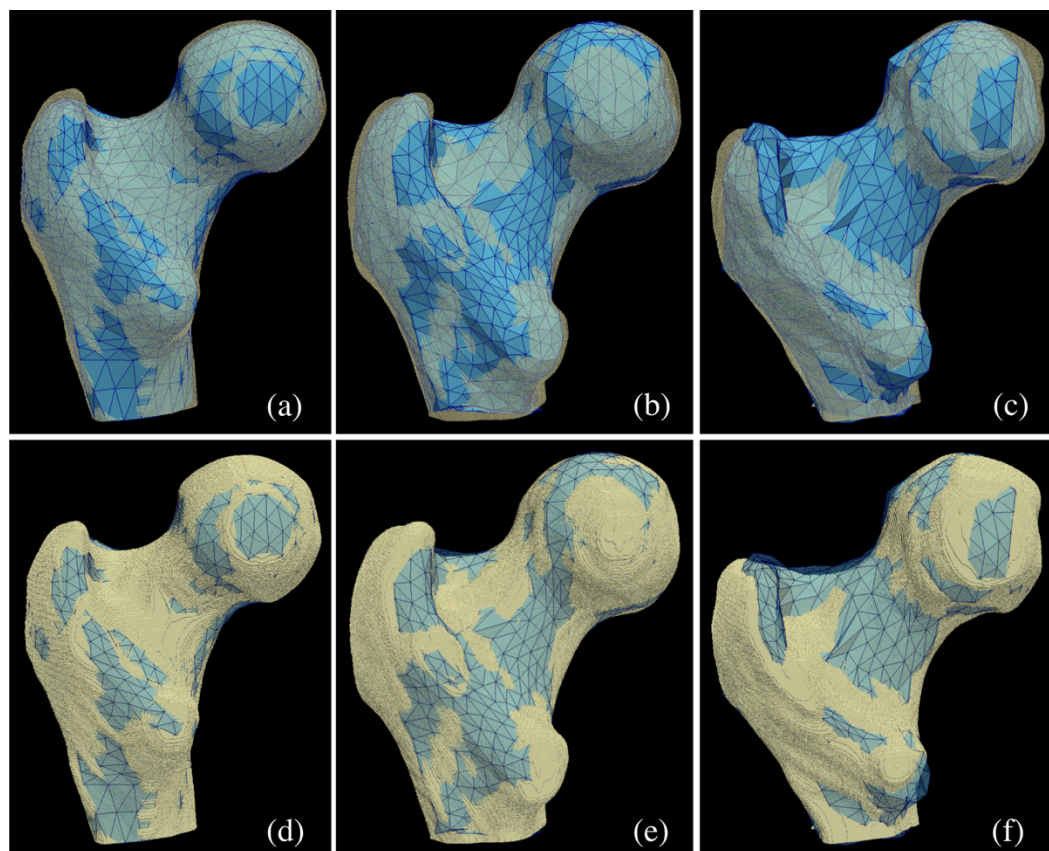
Figure 10. Examples of optimized ASM fitting on the image voxel representation of target femur bone surfaces. Left-to-right: Examples with low (0.270 mm), medium (0.577 mm) and high (1.155 mm) matching errors. Top-row: Three-dimensional surface renditions with high transparency for voxel surface. Bottom-row: Three-dimensional surface renditions with high transparency for landmark mesh surface.

CHAPTER 4
CONCLUSION

An MRI-based shape model of the human femur bone has been developed. The framework of fiducial and secondary landmark allows reliable computation of statistical shape models for complex 3-D anatomic structures. Automatic generation of secondary landmarks using the correspondence of fiducial landmarks and the geodesic elastic deformation of landmark mesh is feasible, and it effectively improves the efficiency as well as the anatomic spatial correspondence of landmarks among individual training shapes. The notion of cushion values in surface-distance force computation allows to gradually pull the secondary landmark mesh on to the target femur bone surface while avoiding any geometric distortion of secondary landmark mesh caused by premature pulling of a landmark on to the target surface and arresting any future deformation of the associated mesh. Also, a novel morphological smoothing algorithm is presented to effectively smooth a femur bone surface reducing digital stair case artifacts caused by relative low resolution of femur bone MRI. Currently, we are advancing this method to automatically generate target regions of interest in individual femur bone shapes. This application will largely reduce expert human time and subjectivity errors in cross-sectional and longitudinal studies.

Long Term Research Goals and Future Directions

Over the last several decades, our laboratory has been working on basic and translational research related to quantitative imaging for bone density, geometry, and micro-architecture ([13], [20]–[23], [25], [26], [28]–[32], [38], [52]–[63]). These research works led the developments of several seminal technologies including digital topological analysis, fuzzy distance approach, tensor scale, which are widely used in bone micro-

structural imaging research ([8], [10], [11], [27], [45], [64]–[82]). The long-term objectives of this research program are two-fold – (1) use ASM based surface landmark correspondence to develop a volumetric deformation process establishing the mapping of a specific femur bone volume onto a mean anatomic space and (2) use ASM to automatically segment the femur bone volume in hip MRI. The first goal will play crucial roles in transverse and longitudinal studies to define anatomically consistent regions of interest (ROIs) for computation of summary measurements. The second goal will reduce expert time and eliminate user-dependent subjective errors in the target bone segmentation. Finally, research efforts will be dedicated to further improve the algorithm for shape optimization on a segmented femur bone surface from a pre-computed ASM.

REFERENCES

[1]   B. L. Riggs and L. J. Melton, "Bone turnover matters: The raloxifene treatment paradox of dramatic decreases in vertebral fractures without commensurate increases in bone density," *Journal of Bone and Mineral Research*, vol. 17, no. 1, pp. 11–14, 2002.

[2]   S. Khosla, B. L. Riggs, E. J. Atkinson, A. L. Oberg, L. J. McDaniel, M. Holets, J. M. Peterson, and L. J. Melton, "Effects of sex and age on bone microstructure at the ultradistal radius: A population-based noninvasive in vivo assessment," *J. Bone Miner. Res.*, vol. 21, no. 1, pp. 124–131, 2006.

[3]   B. L. Riggs, S. Khosla, and L. J. Melton, "Better tools for assessing osteoporosis," *Journal of Clinical Investigation*, vol. 122, no. 12. pp. 4323–4324, 2012.

[4]   TWHO, "Aging and Osteoporosis," *Bulletin*, 1999.

[5]   L. J. Melton, E. A. Chrischilles, C. Cooper, A. W. Lane, and B. L. Riggs, "Perspective how many women have osteoporosis?," *J. Bone Miner. Res.*, vol. 7, no. 9, pp. 1005–1010, 1992.

[6]   S. R. Cummings and L. J. Melton, "Epidemiology and outcomes of osteoporotic fractures.," *Lancet*, vol. 359, no. 9319, pp. 1761–7, 2002.

[7]   B. L. Riggs and L. J. Melton, "Epidemiology of fractures," in *Osteoporosis: Etiology, Diagnosis, and Management*, New York: Raven Press, 1988, pp. 133–154.

[8]   F. W. Wehrli, B. R. Gomberg, P. K. Saha, H. K. Song, S. N. Hwang, and P. J. Snyder, "Digital topological analysis of in vivo magnetic resonance microimages of trabecular bone reveals structural implications of osteoporosis," *J. Bone Miner. Res.*, vol. 16, no. 8, pp. 1520–1531, 2001.

[9]   S. Majumdar, "Magnetic resonance imaging of trabecular bone structure," *Topics in Magnetic Resonance Imaging*, vol. 13, no. 5. pp. 323–334, 2002.

[10]   F. W. Wehrli, P. K. Saha, B. R. Gomberg, H. K. Song, P. J. Snyder, M. Benito, A. Wright, and R. Weening, "Role of magnetic resonance for assessing structure and function of trabecular bone.," *Top. Magn. Reson. Imaging*, vol. 13, no. 5, pp. 335–355, 2002.

[11]   G. Chang, S. K. Pakin, M. E. Schweitzer, P. K. Saha, and R. R. Regatte, "Adaptations in trabecular bone microarchitecture in olympic athletes determined by 7T MRI," *J. Magn. Reson. Imaging*, vol. 27, no. 5, pp. 1089–1095, 2008.

[12]   S. Boutroy, M. L. Bouxsein, F. Munoz, and P. D. Delmas, "In vivo assessment of trabecular bone microarchitecture by high-resolution peripheral quantitative computed tomography.," *J. Clin. Endocrinol. Metab.*, vol. 90, no. 12, pp. 6508–15, 2005.

[13] P. K. Saha, Y. Liu, C. Chen, D. Jin, E. M. Letuchy, Z. Xu, R. E. Amelon, T. L. Burns, J. C. Torner, S. M. Levy, and C. A. Calarge, "Characterization of trabecular bone plate-rod microarchitecture using multirow detector CT and the tensor scale: Algorithms, validation, and applications to pilot human studies," *Med. Phys.*, vol. 42, no. 9, pp. 5410–5425, 2015.

[14] A. M. Parfitt, C. H. E. Mathews, A. B. Villanueva, M. Kleerekoper, B. Frame, and D. S. Rao, "Relationships between surface, volume, and thickness of iliac trabecular bone in aging and in osteoporosis. Implications for the microanatomic and cellular mechanisms of bone loss," *J. Clin. Invest.*, vol. 72, no. 4, pp. 1396–1409, 1983.

[15] A. Vesterby, H. J. G. Gundersen, and F. Melsen, "Star volume of marrow space and trabeculae of the first lumbar vertebra: Sampling efficiency and biological variation," *Bone*, vol. 10, no. 1, pp. 7–13, 1989.

[16] T. Hildebrand and P. Rüegsegger, "Quantification of bone microarchitecture with the structure model index," *Comput. Methods Biomech. Biomed. Engin.*, vol. 1, no. 1, pp. 15–23, 1997.

[17] L. A. Feldkamp, S. A. Goldstein, M. A. Parfitt, G. Jesion, and M. Kleerekoper, "The direct examination of three???dimensional bone architecture in vitro by computed tomography," *J. Bone Miner. Res.*, vol. 4, no. 1, pp. 3–11, 1989.

[18] M. Kleerekoper, A. R. Villanueva, J. Stanciu, D. S. Rao, and A. M. Parfitt, "The role of three-dimensional trabecular microstructure in the pathogenesis of vertebral compression fractures," *Calcif. Tissue Int.*, vol. 37, no. 6, pp. 594–597, 1985.

[19] R. R. Recker, "Architecture and vertebral fracture.," *Calcif. Tissue Int.*, vol. 53 Suppl 1, pp. S139–S142, 1993.

[20] P. K. Saha and B. B. Chaudhuri, "Detection of 3-D Simple Points for Topology Preserving Transformations with Application to Thinning," *IEEE Trans. Pattern Anal. Mach. Intell.*, vol. 16, no. 10, pp. 1028–1032, 1994.

[21] P. K. Saha and B. B. Chaudhuri, "3D Digital Topology under Binary Transformation with Applications," *Comput. Vis. Image Underst.*, vol. 63, no. 3, pp. 418–429, 1996.

[22] P. K. Saha, B. B. Chaudhuri, and D. D. Majumder, "A new shape preserving parallel thinning algorithm for 3D digital images," *Pattern Recognit.*, vol. 30, no. 12, pp. 1939–1955, 1997.

[23] P. K. Saha, B. R. Gomberg, and F. W. Wehrli, "Three-dimensional digital topological characterization of cancellous bone architecture," *Int. J. Imaging Syst. Technol.*, vol. 11, no. 1, pp. 81–90, 2000.

[24] M. Stauber and R. Müller, "Volumetric spatial decomposition of trabecular bone into rods and plates - A new method for local bone morphometry," *Bone*, vol. 38, no. 4, pp. 475–484, 2006.

[25] X. S. Liu, P. Sajda, P. K. Saha, F. W. Wehrli, G. Bevill, T. M. Keaveny, and X. E. Guo, "Complete volumetric decomposition of individual trabecular plates and rods and its morphological correlations with anisotropic elastic moduli in human trabecular bone," *J. Bone Miner. Res.*, vol. 23, no. 2, pp. 223–235, 2008.

[26] P. K. Saha, Y. Xu, H. Duan, A. Heiner, and G. Liang, "Volumetric topological analysis: A novel approach for trabecular bone classification on the continuum between plates and rods," *IEEE Trans. Med. Imaging*, vol. 29, no. 11, pp. 1821–1838, 2010.

[27] C. Chen, X. Zhang, J. Guo, D. Jin, E. M. Letuchy, T. L. Burns, S. M. Levy, E. A. Hoffman, and P. K. Saha, "Quantitative imaging of peripheral trabecular bone microarchitecture using MDCT," *Med. Phys.*, vol. 45, no. 1, pp. 236–249, 2018.

[28] P. K. Saha, F. W. Wehrli, and B. R. Gomberg, "Fuzzy distance transform: Theory, algorithms, and applications," *Comput. Vis. Image Underst.*, vol. 86, no. 3, pp. 171–190, 2002.

[29] P. K. Saha and F. W. Wehrli, "Measurement of Trabecular Bone Thickness in the Limited Resolution Regime of In Vivo MRI by Fuzzy Distance Transform," *IEEE Trans. Med. Imaging*, vol. 23, no. 1, pp. 53–62, 2004.

[30] Y. Liu, D. Jin, C. Li, K. F. Janz, T. L. Burns, J. C. Torner, S. M. Levy, and P. K. Saha, "A robust algorithm for thickness computation at low resolution and its application to in Vivo trabecular bone CT imaging," *IEEE Trans. Biomed. Eng.*, vol. 61, no. 7, pp. 2057–2069, 2014.

[31] P. K. Saha, D. Jin, Y. Liu, G. E. Christensen, and C. Chen, "Fuzzy Object Skeletonization: Theory, Algorithms, and Applications," *IEEE Transactions on Visualization and Computer Graphics*, 2017, in press.

[32] P. K. Saha and F. W. Wehrli, "A robust method for measuring trabecular bone orientation anisotropy at in vivo resolution using tensor scale," *Pattern Recognit.*, vol. 37, no. 9, pp. 1935–1944, 2004.

[33] T. F. Cootes, C. J. Taylor, D. H. Cooper, and J. Graham, "Active Shape Models-Their Training and Application," *Comput. Vis. Image Underst.*, vol. 61, no. 1, pp. 38–59, 1995.

[34] X. Zhang, C. Chen, S. Boone, V. Joshi, A. Welbeck, G. Liang, G. Chang, and P. K. Saha, "MRI-based active shape model of the human proximal femur using fiducial and secondary landmarks and its validation," in *Medical Imaging 2018: Biomedical Applications in Molecular, Structural, and Functional Imaging*, 2018, vol. 10578, p. 105781L.

[35] A. Kelemen, G. Székely, and G. Gerig, "Elastic model-based segmentation of 3-D neuroradiological data sets," *IEEE Trans. Med. Imaging*, vol. 18, no. 10, pp. 828–839, 1999.

[36] D. Rueckert, A. F. Frangi, and J. A. Schnabel, "Automatic construction of 3D statistical deformation models using non-rigid registration," in *Lecture Notes in Computer Science (including subseries Lecture Notes in Artificial Intelligence and Lecture Notes in Bioinformatics)*, 2001, vol. 2208, pp. 77–84.

[37] R. H. Davies, C. J. Twining, T. F. Cootes, J. C. Waterton, and C. J. Taylor, "A minimum description length approach to statistical shape modeling," in *IEEE Transactions on Medical Imaging*, 2002, vol. 21, no. 5, pp. 525–537.

[38] P. K. Saha, J. K. Udupa, and D. Odhner, "Scale-based fuzzy connected image segmentation: Theory, algorithms, and validation," *Comput. Vis. Image Underst.*, vol. 77, no. 2, pp. 145–174, 2000.

[39] P. K. Saha and J. K. Udupa, "Optimum image thresholding via class uncertainty and region homogeneity," *IEEE Trans. Pattern Anal. Mach. Intell.*, vol. 23, no. 7, pp. 689–706, 2001.

[40] S. P. Raya and J. K. Udupa, "Shape-Based Interpolation of Multidimensional Objects," *IEEE Trans. Med. Imaging*, vol. 9, no. 1, pp. 32–42, 1990.

[41] P. K. Saha, R. Strand, and G. Borgefors, "Digital Topology and Geometry in Medical Imaging: A Survey," *IEEE Trans. Med. Imaging*, vol. 34, no. 9, pp. 1940–1964, 2015.

[42] P. K. Saha, G. Liang, J. M. Elkins, A. Coimbra, L. T. Duong, D. S. Williams, and M. Sonka, "A new osteophyte segmentation algorithm using the partial shape model and its applications to rabbit femur anterior cruciate ligament transection via micro-CT imaging," *IEEE Trans. Biomed. Eng.*, vol. 58, no. 8, pp. 2212–2227, 2011.

[43] P. K. Saha, G. Borgefors, and G. Sanniti di Baja, "A survey on skeletonization algorithms and their applications," *Pattern Recognit. Lett.*, vol. 76, pp. 3–12, 2016.

[44] C. Goodall, "Procrustes methods in the statistical analysis of shape," *Journal of the Royal Statistical Society*, vol. 53, no. 2. pp. 285–339, 1991.

[45] G. Chang, C. S. Rajapakse, C. Chen, A. Welbeck, K. Egol, R. R. Regatte, P. K. Saha, and S. Honig, "3-T MR Imaging of Proximal Femur Microarchitecture in Subjects with and without Fragility Fracture and Nonosteoporotic Proximal Femur Bone Mineral Density," *Radiology*, vol. 287, no. 2, pp. 608–619, 2018.

[46] G. Chang, C. M. Deniz, S. Honig, C. S. Rajapakse, K. Egol, R. R. Regatte, and R. Brown, "Feasibility of three-dimensional MRI of proximal femur microarchitecture at 3 tesla using 26 receive elements without and with parallel imaging," *Journal of Magnetic Resonance Imaging*, vol. 40, no. 1. pp. 229–238, 2014.

[47] S. M. Wright and L. L. Wald, "Theory and application of array coils in MR spectroscopy," in *NMR in Biomedicine*, 1997, vol. 10, no. 8, pp. 394–410.

[48] G. C. Wiggins, C. Triantafyllou, A. Potthast, A. Reykowski, M. Nittka, and L. L. Wald, "32-Channel 3 tesla receive-only phased-array head coil with soccer-ball element geometry," *Magn. Reson. Med.*, vol. 56, no. 1, pp. 216–223, 2006.

[49] G. Chang, C. S. Rajapakse, J. S. Babb, S. P. Honig, M. P. Recht, and R. R. Regatte, "In vivo estimation of bone stiffness at the distal femur and proximal tibia using ultra-high-field 7-Tesla magnetic resonance imaging and micro-finite element analysis," *J. Bone Miner. Metab.*, vol. 30, no. 2, pp. 243–251, 2012.

[50] G. Chang, C. S. Rajapakse, M. Diamond, S. Honig, M. P. Recht, D. S. Weiss, and R. R. Regatte, "Micro-finite element analysis applied to high-resolution MRI reveals improved bone mechanical competence in the distal femur of female pre-professional dancers," *Osteoporosis International*, vol. 24, no. 4. pp. 1407–1417, 2013.

[51] G. Chang, S. Honig, R. Brown, C. M. Deniz, K. a Egol, J. S. Babb, R. R. Regatte, and C. S. Rajapakse, "Finite Element Analysis Applied to 3-T MR Imaging of Proximal Femur Microarchitecture: Lower Bone Strength in Patients with Fragility Fractures Compared with Control Subjects," *Radiology*, vol. 272, no. 2, pp. 464–474, 2014.

[52] P. K. Saha, S. Basu, and E. A. Hoffman, "Multiscale opening of conjoined fuzzy objects: Theory and applications," *IEEE Trans. Fuzzy Syst.*, vol. 24, no. 5, pp. 1121–1133, 2016.

[53] D. Jin, K. S. Iyer, C. Chen, E. A. Hoffman, and P. K. Saha, "A robust and efficient curve skeletonization algorithm for tree-like objects using minimum cost paths," *Pattern Recognit. Lett.*, vol. 76, pp. 32–40, 2016.

[54] C. Li, D. Jin, C. Chen, E. M. Letuchy, K. F. Janz, T. L. Burns, J. C. Torner, S. M. Levy, and P. K. Saha, "Automated cortical bone segmentation for multirow-detector CT imaging with validation and application to human studies," *Med. Phys.*, vol. 42, no. 8, pp. 4553–4565, 2015.

[55] R. Strand, K. C. Ciesielski, F. Malmberg, and P. K. Saha, "The minimum barrier distance," *Comput. Vis. Image Underst.*, vol. 117, no. 4, pp. 429–437, 2013.

[56] M. J. Wald, B. Vasilic, P. K. Saha, and F. W. Wehrli, "Spatial autocorrelation and mean intercept length analysis of trabecular bone anisotropy applied to in vivo magnetic resonance imaging," *Med. Phys.*, vol. 34, no. 3, pp. 1110–1120, 2007.

[57] X. S. Liu, P. Sajda, P. K. Saha, F. W. Wehrli, and X. E. Guo, "Quantification of the roles of trabecular microarchitecture and trabecular type in determining the elastic modulus of human trabecular bone," *J. Bone Miner. Res.*, vol. 21, no. 10, pp. 1608–1617, 2006.

[58]   P. K. Saha, "Tensor scale: A local morphometric parameter with applications to computer vision and image processing," *Comput. Vis. Image Underst.*, vol. 99, no. 3, pp. 384–413, 2005.

[59]   J. K. Udupa and P. K. Saha, "Fuzzy connectedness and image segmentation," in *Proceedings of the IEEE*, 2003, vol. 91, no. 10, pp. 1649–1669.

[60]   J. K. Udupa, P. K. Saha, and R. A. Lotufo, "Relative fuzzy connectedness and object definition: Theory, algorithms, and applications in image segmentation," *IEEE Trans. Pattern Anal. Mach. Intell.*, vol. 24, no. 11, pp. 1485–1500, 2002.

[61]   P. K. Saha and J. K. Udupa, "Fuzzy connected object delineation: Axiomatic path strength definition and the case of multiple seeds," *Comput. Vis. Image Underst.*, vol. 83, no. 3, pp. 275–295, 2001.

[62]   B. R. Gomberg, P. K. Saha, H. K. Song, S. N. Hwang, and F. W. Wehrli, "Topological analysis of trabecular bone MR images.," *IEEE Trans. Med. Imaging*, vol. 19, no. 3, pp. 166–74, 2000.

[63]   P. K. Saha, B. B. Chaudhuri, B. Chanda, and D. Dutta Majumder, "Topology preservation in 3D digital space," *Pattern Recognit.*, vol. 27, no. 2, pp. 295–300, 1994.

[64]   L. M. Griffin, S. Honig, C. Chen, P. K. Saha, R. Regatte, and G. Chang, "7T MRI of distal radius trabecular bone microarchitecture: How trabecular bone quality varies depending on distance from end-of-bone," *J. Magn. Reson. Imaging*, vol. 45, no. 3, pp. 872–878, 2017.

[65]   C. Chen, D. Jin, Y. Liu, F. W. Wehrli, G. Chang, P. J. Snyder, R. R. Regatte, and P. K. Saha, "Trabecular bone characterization on the continuum of plates and rods using in vivo MR imaging and volumetric topological analysis," *Phys. Med. Biol.*, vol. 61, no. 18, pp. N478–N496, 2016.

[66]   S. Dudley-Javoroski, M. A. Petrie, C. L. McHenry, R. E. Amelon, P. K. Saha, and R. K. Shields, "Bone architecture adaptations after spinal cord injury: impact of long-term vibration of a constrained lower limb.," *Osteoporos. Int.*, vol. 27, no. 3, pp. 1149–1160, 2016.

[67]   A. Hotca, C. S. Rajapakse, C. Cheng, S. Honig, K. Egol, R. R. Regatte, P. K. Saha, and G. Chang, "In vivo measurement reproducibility of femoral neck microarchitectural parameters derived from 3T MR images," *J. Magn. Reson. Imaging*, vol. 42, no. 5, pp. 1339–1345, 2015.

[68]   G. Chang, S. Honig, Y. Liu, C. Chen, K. K. Chu, C. S. Rajapakse, K. Egol, D. Xia, P. K. Saha, and R. R. Regatte, "7 Tesla MRI of bone microarchitecture discriminates between women without and with fragility fractures who do not differ by bone mineral density," *J. Bone Miner. Metab.*, vol. 33, no. 3, pp. 285–293, 2015.

[69]   S. Dudley-Javoroski, R. Amelon, Y. Liu, P. K. Saha, and R. K. Shields, "High bone density masks architectural deficiencies in an individual with spinal cord injury," *J. Spinal Cord Med.*, vol. 37, no. 3, pp. 349–354, 2014.

[70]   S. Dudley-Javoroski, P. K. Saha, G. Liang, C. Li, Z. Gao, and R. K. Shields, "High dose compressive loads attenuate bone mineral loss in humans with spinal cord injury," *Osteoporos. Int.*, vol. 23, no. 9, pp. 2335–2346, 2012.

[71]   G. Chang, L. Wang, G. Liang, J. S. Babb, P. K. Saha, and R. R. Regatte, "Reproducibility of subregional trabecular bone micro-architectural measures derived from 7-Tesla magnetic resonance images," *Magn. Reson. Mater. Physics, Biol. Med.*, vol. 24, no. 3, pp. 121–125, 2011.

[72]   S. C. B. Lam, M. J. Wald, C. S. Rajapakse, Y. Liu, P. K. Saha, and F. W. Wehrli, "Performance of the MRI-based virtual bone biopsy in the distal radius: Serial reproducibility and reliability of structural and mechanical parameters in women representative of osteoporosis study populations," *Bone*, vol. 49, no. 4, pp. 895–903, 2011.

[73]   G. Chang, L. Wang, G. Liang, J. S. Babb, G. C. Wiggins, P. K. Saha, and R. R. Regatte, "Quantitative assessment of trabecular bone micro-architecture of the wrist via 7 Tesla MRI: Preliminary results," *Magn. Reson. Mater. Physics, Biol. Med.*, vol. 24, no. 4, pp. 191–199, 2011.

[74]   F. W. Wehrli, G. A. Ladinsky, C. Jones, M. Benito, J. Magland, B. Vasilic, A. M. Popescu, B. Zemel, A. J. Cucchiara, A. C. Wright, H. K. Song, P. K. Sana, H. Peachey, and P. J. Snyder, "In vivo magnetic resonance detects rapid remodeling changes in the topology of the trabecular bone network after menopause and the protective effect of estradiol," *J. Bone Miner. Res.*, vol. 23, no. 5, pp. 730–740, 2008.

[75]   G. A. Ladinsky, B. Vasilic, A. M. Popescu, M. Wald, B. S. Zemel, P. J. Snyder, L. Loh, K. S. Hee, P. K. Saha, A. C. Wright, and F. W. Wehrli, "Trabecular structure quantified with the MRI-based virtual bone biopsy in postmenopausal women contributes to vertebral deformity burden independent of areal vertebral BMD," *J. Bone Miner. Res.*, vol. 23, no. 1, pp. 64–74, 2008.

[76]   F. W. Wehrli, H. K. Song, P. K. Saha, and A. C. Wright, "Quantitative MRI for the assessment of bone structure and function," *NMR in Biomedicine*, vol. 19, no. 7. pp. 731–764, 2006.

[77]   C. E. Jones, R. L. Wolf, J. A. Detre, B. Das, P. K. Saha, J. Wang, Y. Zhang, H. K. Song, A. C. Wright, E. M. Mohler, R. M. Fairman, E. L. Zager, O. C. Velasquez, M. A. Golden, J. P. Carpenter, and F. W. Wehrli, "Structural MRI of carotid artery atherosclerotic lesion burden and characterization of hemispheric cerebral blood flow before and after carotid endarterectomy," *NMR Biomed.*, vol. 19, no. 2, pp. 198–208, 2006.

[78] B. R. Gomberg, P. K. Saha, and F. W. Wehrli, "Method for cortical bone structural analysis from magnetic resonance images," *Acad. Radiol.*, vol. 12, no. 10, pp. 1320–1332, 2005.

[79] F. W. Wehrli, M. B. Leonard, P. K. Saha, and B. R. Gomberg, "Quantitative high-resolution magnetic resonance imaging reveals structural implications of renal osteodystrophy on trabecular and cortical bone.," *J. Magn. Reson. Imaging*, vol. 20, no. 1, pp. 83–9, 2004.

[80] B. R. Gomberg, F. W. Wehrli, B. Vasilić, R. H. Weening, P. K. Saha, H. K. Song, and A. C. Wright, "Reproducibility and error sources of μ-MRI-based trabecular bone structural parameters of the distal radius and tibia," *Bone*, vol. 35, no. 1, pp. 266–276, 2004.

[81] F. W. Wehrli, P. K. Saha, B. R. Gomberg, and H. K. Song, "Noninvasive assessment of bone architecture by magnetic resonance micro-imaging-based virtual bone biopsy," in *Proceedings of the IEEE*, 2003, vol. 91, no. 10, pp. 1520–1541.

[82] B. R. Gomberg, P. K. Saha, and F. W. Wehrli, "Topology-based orientation analysis of trabecular bone networks," *Med. Phys.*, vol. 30, no. 2, pp. 158–168, 2003.